Structure-Based Intensity Propagation for 3-D Brain Reconstruction With Multilayer Section Microscopy

Haoyi Liang, Natalia Dabrowska, Jaideep Kapur, and Daniel S. Weller

***Abstract*— Microscopy is widely used for brain research because of its high resolution and ability to stain for many different biomarkers. Since whole brains are usually sectioned for tissue staining and imaging, reconstruction of 3D brain volumes from these sections is important for visualization and analysis. Recently developed tissue clearing techniques and advanced confocal microscopy enable multilayer sections to be imaged without compromising the resolution. However, noticeable structure inconsistence occurs if surface layers are used to align these sections. In this paper, a structure-based intensity propagation method is designed for the robust representation of multilayer sections. The 3D structures in reconstructed brains are more consistent using the proposed methods. Experiments are conducted on 367 multilayer sections from 20 mouse brains. The average reconstruction quality measured by the structure consistence index increases by 45% with the tissue flattening method and 29% further with the structure-based intensity propagation.**

***Index Terms*— Brain reconstruction, confocal microscopy, registration.**

I. Introduction

BIOMEDICAL images are significant to biology and medical science. Although other imaging techniques, such as magnetic resonance imaging (MRI) and computed tomography (CT), are valuable noninvasive imaging approaches, microscopy remains irreplaceable because of its high resolution [1]–[5] and the flexible choice of stains [6]–[9]. As one of the most sophisticated organs, brains consist of intricate structures and diversified cells. Microscopy enables comprehensive observation of brain histology and activity [6], [7], [10], [11]. However, a whole brain usually is sectioned into slices for high resolution imaging. Reconstructed 3D virtual brains benefit brain-related research in three aspects: visualization, anatomical labeling, and 3D measurement. One of the main goals of the Allen Brain Atlas (ABA) project is allowing researchers to make comprehensive queries about gene expression patterns in 3D with reconstructed brains [6]. Visualizing the neuron morphology in reconstructed brains relaxes the view angle limit caused by physical sectioning, and is crucial to understand the communication of neural signals [12], [13]. Atlas-matching provides critical anatomical information of the imaged brain activities. However, the deviation between the actual cutting plane and the standard cutting planes would compromise the registration accuracy. With 3D reconstruction of brain volumes, a 2D cross-section view from any angle is possible and thus leads to more accurate anatomy labeling [3], [14], [15]. Because of the importance of 3D brain volumes, many brain atlases provide 3D brain reference and gene expression patterns, such as Allen brain atlas [6], Hof's brain atlas [16] and Paxinos & Franklin's brain atlas [17]. Accurate 3D measurements for diagnosis and pathology study are also facilitated by the reconstructed brain volumes [12], [18], [19]. The activation pattern of grid cells in the hippocampus plays an important role in memory formation and environment recognition [20]–[22]. Extending this pattern analysis from 2D to 3D with reconstructed brain volumes is helpful to further understand the underlying mechanism [20]. For this paper, brain tissues collected from mice expressing fluorescent tdTomato and co-labeled with the neuronal marker NeuN, are imaged. The reconstructed brain volumes provide details about seizure spreading at multiple scales: from circuits, systems, to the whole brain. The seizure spreading pathways are helpful for neuroscientists to find the neurobiological basis for the use of drugs to terminate status epilepticus at an early stage.

Existing brain reconstruction works can be classified into two approaches by the way that specimens are sliced and imaged [9]: reconstruction with single-layer sections [23]–[27] and reconstruction with multilayer sections [9], [12], [28]–[31]. Imaging and reconstruction with multilayer sections are getting more attention recently because of the less labor required for the tissue preparation [9], [28] and the greater robustness to distortions such as warping and tearing.

Manuscript received August 15, 2018; revised October 22, 2018; accepted October 24, 2018. Date of publication October 29, 2018; date of current version May 1, 2019. The work of H. Liang was supported by the Presidential Fellowship for Collaborative Neuroscience, University of Virginia. The work of J. Kapur was supported by NIH under Grant R01 NS040337-13 and Grant NIH R01 NS044370-12. The work of D. S. Weller was supported in part by NIH under Grant R21 EB022309 and in part by the Thomas F. and Kate Miller Jeffress Memorial Trust, Bank of America, Trustee. *(Corresponding author: Haoyi Liang.)*

H. Liang and D. S. Weller are with the Department of Electrical and Computer Engineering, University of Virginia, Charlottesville, VA 22904 USA

N. Dabrowska and J. Kapur are with the Department of Neurology, University of Virginia, Charlottesville, VA 22904 USA

This paper has supplementary downloadable multimedia material available at http://ieeexplore.ieee.org provided by the authors. This includes a document of the implementation details, and animations for two reconstructed brains with four different methods. This material is 121 MB in size.

Color versions of one or more of the figures in this paper are available online at http://ieeexplore.ieee.org.

Digital Object Identifier 10.1109/TMI.2018.2878488

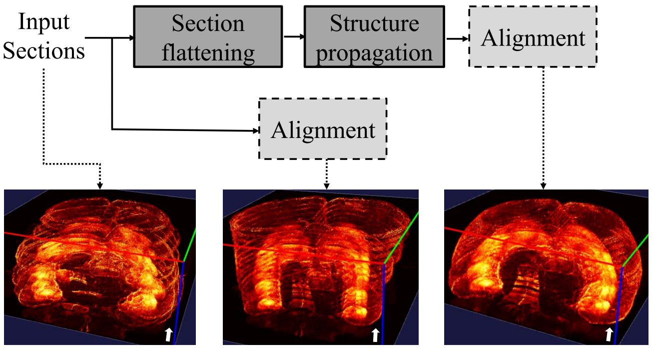

Fig. 1. The top row is the reconstruction pipeline adopted in this work. Section flattening and structure propagation are the two techniques proposed to improve the reconstruction quality. The three figures at the bottom row are the stacked raw sections, the reconstructed brain without the proposed techniques, and the reconstructed brain with the proposed techniques. The arrows in the three bottom figures indicate the ventral-dorsal direction.

For this paper, multilayer sections are the raw data for whole brain reconstruction. Our previous work in [32] describes an automatic tissue flattening method to remove the warping artifacts along the cutting axis in multilayer sections. The reconstructed brains are more compact with flattened sections, but the structure inconsistence and the cylindrical artifact [28] still exist as shown in Fig. 1.

Numerous methods are proposed to improve the structure consistence and to eliminate the cylindrical artifact for brain reconstruction. Extra equipment, such as high-resolution MRI scanners [23], [24], and algorithms imposing smoothness constraints [25]–[27], are two common approaches. Among these methods, the best reference selection (BRS) [25] proposes an interesting idea: registering a section to its nearest key section, rather than directly to the previous one. The key sections are selected by criteria such as contrast, entropy and intensity [25]. A similar idea is also explored in [24].

Inspired by the previous works [24], [25], structure-based intensity propagation (SIP) is proposed to improve the structure consistence of brain reconstruction. Different from BRS [25], the references used for registration are created by propagation, rather than selected as in BRS. Fig. 1 illustrates the overall work flow. This work obtains robust representatives of multilayer sections with modules of tissue flattening and structure propagation. By feeding the alignment module with better representatives of multilayer sections, SIP improves the reconstruction quality in two aspects. First, the structure transition among sections is smoother because the structural trend within each 3D section is accurately reflected in propagated surfaces. Secondly, the flip detection is more reliable. Since brain structures are highly symmetric on coronal and horizontal planes, automatic flip detection is challenging. The proposed structure-based intensity propagation facilitates flip detection by enhancing the signal intensity and structure contrast.

The rest of this paper is organized as follows. Section II summarizes existing brain reconstruction works, and then introduces the brain registration pipeline adopted in this paper. Section III reviews the tissue flattening method in [32], and then elaborates on the proposed structure-based intensity propagation. In Section IV, experiments demonstrate how the proposed methods improve the quality of the brain reconstruction. At last, Section V reviews the novelty and experimental verification of the proposed methods, and discusses the further work of brain reconstruction.

II. RECONSTRUCTION BACKGROUNDS

A. Existing Brain Reconstruction Works

As mentioned in Section I, brain reconstruction can be classified into two approaches according to the number of layers in each section. Although the specimen preparation procedures are different for single-layer sections and multilayer sections, the following reconstruction shares similar frameworks and faces some common challenges.

Compared with multilayer sections, each single-layer section is easier to prepare and image. The typical thickness of single-layer sections is between 10 to 100 microns [23]–[27], and each physical section is imaged with a single 2D image. However, the preparation of a high-quality single-layer section is challenging and time-consuming [24], [25], [27], [28], [31]. In [24], exhaustive pre-processing, such as visual quality inspection and mask detection, is required before registration. After imaging these sections, the major challenge is maintaining the smoothness of the reconstructed brains. Accurate section-to-section registrations cannot avoid the cylindrical artifacts due to the aperture problem [28], [33]: minor registration errors accumulate along the z-direction and compromise the overall shape of the reconstructed volume. In [3], [23], and [24], MRI scanners image the overall shapes of brains before slicing. Some algorithms are designed by optimizing the registration order [24], [25] or applying smoothness constraints [26], [27].

The brain reconstruction with multilayer sections [9], [12], [27], [29] is getting additional attention because of two techniques: tissue clearing and high resolution confocal microscopy. Lipids are removed with tissue clearing [5], [12], [34]–[37], and thus the light emitted by fluorescent markers undergoes less scattering. Advanced confocal microscopy enables specimens to be imaged at different depth without the compromise of resolution. However, reconstruction with multilayer sections has its own unique challenges. As one of the important steps during specimen preparation, the tissue clearing turns specimens both transparent and warped. How to select proper 2D representatives of multilayer sections for registration is difficult. For single-layer sections, one physical section is directly used for registration, while the surface layers in a raw multilayer section are not good choices for registration. Due to the distortions during tissue preparation and the partial volume effect during imaging, the surface layers do not precisely reflect the intra-section structural trends. To solve this challenge, existing reconstruction methods with multilayer sections either rely on manually labeled information or highly customized equipment. Manually selected key points on tissue surfaces are used as 2D representatives of multilayer sections for registration [9], [12], [30], [31], [38]. Traced neuron features in an interactive GUI are used for

3D volume reconstruction in [12], [30], and [38]. However, this laborious approach is not scalable. Alternatively, customized equipment is assembled to facilitate the reconstruction process [12], [28]. In [12] and [28], the confocal microscope is integrated with a vibrating microtome. The sophisticated assembly procedures and customization required limit their applications. For example, staining is done before slicing in [12], and thus many organic immunohistochemical stains cannot be used due to the limits of the penetration depth.

At last, although light-sheet microscopy together with tissue clearing techniques is technically possible to image the whole brain without any slicing, such whole brain imaging is constrained by the choice of stains and the resolution [19]. Many antibodies and stains do not penetrate through the whole intact brain. Also, the resolution of a typical light-sheet microscope is not enough to resolve individual cells, while in-plane resolution under 1 μm is common for point scanning microscopes such as two-photon or confocal microscopy.

B. Alignment Pipeline in This Paper

As stated in Section I, the brain reconstruction pipelines for single-layer and multilayer sections are all based on section-to-section registration. In this work, a three-step registration pipeline is implemented with rough alignment, affine transformation and non-rigid registration. Our proposed structure correction methods do not rely on particular registration methods. The works [39]–[41] are selected because of their robust performance and public implementations. The first step, rough alignment, only takes translation and rotation into consideration, and both non-flipped and flipped versions of the section to be registered are evaluated. The parameter sets that achieve highest correlation scores [39] in the non-flipped and flipped versions are saved. The second step, affine registration, maximizes the mutual information [40] of the outputs from rough alignment. The flip status is decided after affine registration: the status that achieves higher mutual information index is selected. Unlike single-layer sections, only one combination of the four flip statuses of two adjacent multilayer sections achieves the highest mutual information. For single-layer sections, if two adjacent sections both are incorrectly flipped, the registration cost is the same as the correct flip situation. However, for multilayer sections, because the top surface and the bottom surface are different, four different flip combinations of two adjacent sections lead to four different registration costs. The last step is non-rigid registration that minimizes the residual complexity [41] between two input images. The resolutions also gradually increase from rough alignment, affine registration to non-rigid registration. Such hierarchical registration approaches are common in brain reconstruction works for the purpose of computation time and registration accuracy [18], [24]. Readers are referred to [32] for details about the implementation.

To apply the registration pipeline for brain reconstruction with multilayer sections, a representative has to be selected. In the next section, the proposed tissue flattening and structure-based intensity propagation provide accurate representatives for the multilayer section registration.

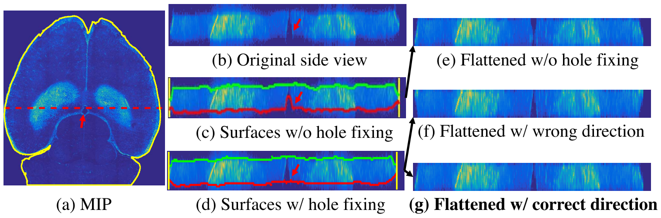
(a) MIP
(b) Original side view
(c) Surfaces w/o hole fixing
(d) Surfaces w/ hole fixing
(e) Flattened w/o hole fixing
(f) Flattened w/ wrong direction
(g) Flattened w/ correct direction

Fig. 2. Intermediate results of tissue flattening. (a) is the maximum intensity projection of one section sliced on the horizontal plane. The dashed line in (a) indicates the positions of side views. (b) is the side view of the raw section. (c) shows the detected surfaces before hole fixing. If the tissue is projected onto the bottom surfaces in (c), the structure around the ventricle is changed as shown in (e). (d) shows the detected surface after hole fixing. However, with incorrect projection direction, structures at the boundaries are altered as shown in (f). With correctly detected surfaces and the projection direction, (g) shows the flattened tissue from (b).

III. PROPOSED STRUCTURE CORRECTION METHODS

The proposed structure correction for brain reconstruction contains two parts: tissue flattening [32] and structure-based intensity propagation. Before tissue flattening, the structures in most layers of a multilayer section are distorted by the unevenness on z-direction. After tissue flattening, the warping artifacts on the z-direction are removed, and the surface layers show the general contours and major structures. However, the structures presented on the surface layers after flattening are not in accord with the intra-section structural trend, and the signal intensity is usually weak. Structure-based intensity propagation is designed to overcome these limitations in surface layers for accurate registration and flip detection.

A. Flattening

The tissue clearing process not only removes the lipids from the specimens, but also slightly warps the specimens. In order to process large numbers of tissues, an automatic tissue flattening method [32] is proposed. Fig. 2 illustrates the key intermediate results of tissue flattening. The warping distortion exists in the raw section as shown in Fig.2(b). Fig. 2(c) shows the detected surface layers with adaptive thresholds. By assuming that the distance between the top and the bottom layers is constant, the hump on the bottom surface is removed in Fig. 2(d) after hole fixing. At last, the projection direction is decided by the total variation along the surface layer rims. The surface with flatter rim is selected as the layer onto which we project the rest of the section. Details about the tissue flattening can be found in [32].

Tissue flattening improves the quality of reconstructed brains in two aspects. First, surface layers, rather than maximum intensity propagation (MIP), of the flattened tissues can be used for registration. The overall shape of reconstructed brains is more natural [32]. Secondly, the wide gaps among sections are removed. However, minor structure inconsistence, such as the zig-zag contour on the brain outline, still exists [32]. Another limitation of tissue flattening is that structure contrast and signal intensity are weak on the surface layers. To overcome these drawbacks, structure-based intensity propagation (SIP) is proposed in the next section.

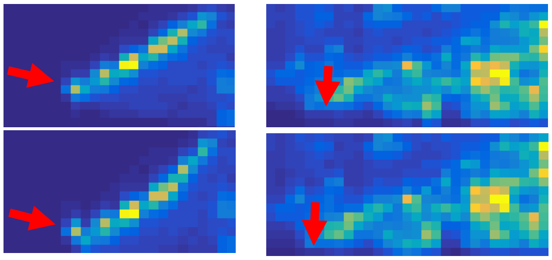
(a) (b)

Fig. 3. First and second rows are the cross-section views of a section before and after flattening. In (a), tissue boundaries are not accurately reflected on the bottom layer because of the upward tilt. In (b), the size of the hippocampus grows from the top to the bottom, but this structural trend is not correctly reflected on the bottom layer.

B. Structure-Based Intensity Propagation

Once obtaining the flattened sections, a straightforward reconstruction scheme registers the surfaces from neighboring sections to each other [9], [12], [28]–[31]. Fig. 3 illustrates why this approach is not suitable for automatic reconstruction. In Fig. 3(a), the flattened patch on the bottom preserves the upwards tilt at the end. Surfaces with such tilts cannot accurately delineate the boundaries, and are the source of the zig-zag artifacts in the reconstructed brains [32]. In Fig. 3(b), the signal strength on the surface layer is weak. One reason for this phenomenon is partial volume imaging on the surfaces. As representatives of a multilayer section, these surfaces with weak signal strength and contrast lead to unstable registration or even flip errors due to mirror symmetry [32]. In order to improve the signal intensity and contrast with intra-section information, one straightforward idea is applying the median or mean filter along the z-direction. The defect of this scheme is that the structure changing along the z-axis is neglected. However, if these filters are applied along the structure directions in the sections, both the aims of signal enhancement and structure preservation are achieved. The proposed structure-based intensity propagation implements the idea of the structure-oriented median filter.

Alg. 1 summarizes the structure-based intensity propagation. The inputs of Alg. 1 are a 3D stack of size $M \times M \times D$ with isotropic resolution and a patch size, N. The width and the height (the first two dimensions) of the input 3D image stack I do not have to be equal. A square 3D stack is used for the simplicity of notation in Alg. 1. If the raw data acquired by confocal microscopy is of anisotropic resolution, the raw data should be scaled so that the 3D stack is of isotropic resolution before fed to Alg. 1. In our implementation, the scaling is done with cubic interpolation [42]. The outputs of Alg. 1 are two 2D images of size $M \times M$, L^{top} and L^{bottom}. These two 2D images are the propagated surfaces to align two adjacent multilayer sections. The steps in Alg. 1 are classified into two parts. The first part, steps 1-6, is structure estimation. The second part, steps 7-10, is surface layer estimation. Fig. 4 illustrates key intermediate results in Alg. 1. Fig. 4(a) is a rendered multilayer section in 3D. The thickness of all the multilayer sections in our experiments is 200 μm, which is also the typical penetration depth of many immunohistochemical stains. The in-plane range of the multilayer section in Fig. 4(a) is 9569×9669 μm^2. Fig. 4(b) and (c) are the outputs of the first module in Alg. 1, F_x and F_y. The estimated structure maps, F_x and F_y, are two 2D maps of size $M \times M$. The expansion direction and magnitude for each in-plane position are characterized in Fig. 4(b) and (c). The MIP of the raw section in Fig. 4(d) cannot differentiate the top and the bottom surfaces, and thus leads to the cylindrical artifact in the reconstructed brain. The bottom surface of the flattened section in Fig. 4(e) has weak signal contrast and loses some asymmetric information that is key to flip detection. The propagated bottom surface in Fig. 4(f) retains both the signal strength and structures. The detailed computational complexity analysis and an optimized implementation of Alg. 1 are provided in the supplementary material.[1] The structure-based intensity propagation is introduced with the implementation in Alg. 1 for its clarity, and the computational complexity of Alg. 1 is $O(M^6 D^2)$. The computational complexity of the optimized implementation in the supplementary material is $O(M^2 D log(MD))$. The following two paragraphs explain the two modules, structure estimation and surface layer estimation, in detail.

Algorithm 1 Structure-Based Intensity Propagation

```
Inputs:
  $I$: 3D image stack of size $M \times M \times D$
  $N$: patch size
Outputs:
  $L^{top}$: Propagated top surface of size $M \times M$
  $L^{bottom}$: Propagated bottom surface of size $M \times M$

Structure Estimation:
  for every $p$ on the imaging plane of size $M \times M$ do
    1. $G(p) = [g_x(p)\ g_y(p)\ g_z(p)]$                ▷ gradient matrix
    2. $U(p)S(p)V(p)^T = SVD(G(p))$                       ▷ SVD
    3. $[v_1(p)\ v_2(p)\ v_3(p)] = V(p)$
    4. $h(p) = \underset{h(p) \perp v_1(p), \|h(p)\|_2^2 = 1}{\operatorname{argmin}} h_z(p)$   ▷ structure vector
    5. $F_x(p) = \frac{h_x(p)}{h_z(p)}$
    6. $F_y(p) = \frac{h_y(p)}{h_z(p)}$
  end for
Surface Layer Estimation:
  for $i = 1 : D$ do
    7. $I_i^{top} = I_i(p_x + F_x \cdot (i-1), p_y + F_y \cdot (i-1))$
    8. $I_i^{bottom} = I_i(p_x - F_x \cdot (D-i), p_y - F_y \cdot (D-i))$
  end for
  9. $L^{top} = median_z(I^{top})$
  10. $L^{bottom} = median_z(I^{bottom})$
```

The outputs of structure estimation are two 2D maps showing the structure changes on two in-plane directions. One assumption of the structure estimation is that the main structures in cross-section views are linear because each multilayer section is thin, as shown in Fig. 4(a). The typical dimension of a multilayer section in our experiment is $10000 \times 10000 \times 200$ μm^3, and thus the depth-to-length ratio is about $1/50$. The first step in Alg. 1 is constructing the gradient matrix,

---

[1] Supplementary materials are available in the supplementary files/ multimedia tab on IEEE Xplore.

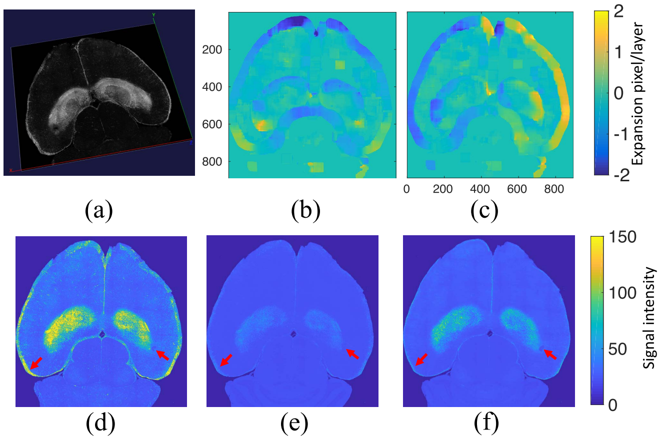

Fig. 4. (a) A rendered multilayer section of size 9569 × 9569 × 200 μm^3 in 3D. This section is sliced on the horizontal plane. From the top to the bottom (on z-direction), the brain and the hippocampus expand. (b) Estimated structure map on the direction of top-bottom in the imaging-plane. (c) Estimated structure map the direction of left-right in the imaging-plane. MIP, the bottom surface of flattened section and the propagated bottom surface are (d), (e) and (f) respectively.

$G(p)$, for each position, p, on the imaging plane. The gradient matrix, $G(p)$, of size $N^2D \times 3$ is composed of three vectors that correspond to gradients along three directions. In our implementation, the gradients at each pixel are computed by a central difference on a $3 \times 3 \times 3$ neighborhood. The singular value decomposition (SVD) of the gradient matrix, $G(p)$, is defined as

$$G = USV^T = U \begin{bmatrix} s_1 & 0 & 0 \\ 0 & s_2 & 0 \\ 0 & 0 & s_3 \end{bmatrix} \begin{bmatrix} v_1 & v_2 & v_3 \end{bmatrix}^T, \quad (1)$$

where U and V are both orthonormal matrices. Vector v_1 is of size 3×1 and corresponds to the dominant direction of the local gradient; v_2 and v_3 are orthogonal to v_1. The three singular values, s_1, s_2 and s_3, represent the amount of gradient variation on the three corresponding singular vectors v_1, v_2 and v_3, and $s_1 > s_2 > s_3$. With the definition of SVD, the dominant intensity changing direction, v_1, is always perpendicular to the main structure direction [43]. Next, the structure direction, h, is estimated by selecting the unit vector that is perpendicular to v_1 and has the largest z-direction descent. This process is reflected in Step 4 in Alg. 1. The property of being perpendicular to v_1 guarantees h lies on the structure surface. Among these vectors, the one that has the largest downward z-direction component is selected as h. The three components in h are h_x, h_y and h_z. The minimization operation in Step 4 of Alg.1 specifies the downward direction of the unit vectors have negative signs. The property of having the largest z-direction component can be interpreted as having the smallest in-plane component because of the first property of being a unit vector. Therefore, when propagating an intra-section voxel to the positions of surface layers, the propagation path with direction h stays on the structure, and has the smallest in-plane displacement. After obtaining the structure direction h, the structure change on xy-planes is calculated in Step 5 and 6 in Alg. 1. The values in $F_x(p)$ and $F_y(p)$ indicate the displacement of a pixel at p traveling to its next layer. In other words, the units of $F_x(p)$ and $F_y(p)$ are pixel/layer. Fig. 4(b) and (c) show the structure change maps.

The second part of Alg. 1 estimates the propagated surfaces with the structure change maps. In Step 7 and Step 8 in Alg. 1, every layer is transformed to positions of the top layer and the bottom layer. The deformation fields, $(p_x + F_x \cdot (i-1), p_y + F_y \cdot (i-1))$ and $(p_x - F_x \cdot (D-i), p_y - F_y \cdot (D-i))$, are calculated with structure changes and the distances to surface layers. Two 3D stacks, I^{top} and I^{bottom}, are created with reference to the top and bottom layers respectively. Ideally, only vertical structures should be presented in the side views of I^{top} and I^{bottom}. At last, median values in the z-direction are taken from I^{top} and I^{bottom} as the propagated surface layers. Fig. 4(f) shows the propagated bottom surface of one multilayer section.

To better interpret how the proposed structure-based intensity propagation works, a 2D example is shown in Fig. 5. The method described in Alg. 1 can be easily applied to 2D cases. The difference is that the surface layers in Alg. 1 are 1D lines in 2D cases. Fig. 5(a) is a 2D patch from the cross-section view of the raw data. The most significant structure in Fig. 5(a) is the boundary of a mouse brain. Two defects in the raw data are presented. First, the position of the boundary on the top line is not accurate. Second, the intensity of the bottom line is weak. Fig. 5(d) plots the gradients in Fig. 5(a) and the fitted ellipse with SVD. The orientation in Fig. 5(d) reflects the direction of the significant structure. The dashed arrow in Fig. 5(a) is equivalent to the normal vector, v_1, in Alg. 1, and the solid arrow is equivalent to the unit structure vector, h, in Alg. 1. Computing the solid arrow in Fig. 5(a) fulfills the structure estimation in Alg. 1, and the next step is the surface layer estimation. Applying the displacement fields to each layer in Alg. 1 is simply shifting each line in the 2D cases. Fig. 5(b) and (c) are the propagated stacks whose counterparts in Alg. 1 are I^{top} and I^{bottom}. At last, applying a median filter to Fig. 5(b) and (c), the propagated top line and the propagated bottom line are obtained. Fig. 5(e) compares the original surface lines and the propagated surface lines. The boundary position is more precisely reflected in the propagated top line, and is more distinct in the propagated bottom line.

IV. EXPERIMENTS

In this section, the data acquisition procedure and the evaluation criteria are first reviewed. Three experiments, section-to-section registration, flip detection and whole brain reconstruction, are conducted to illustrate how the proposed methods improve upon conventional reconstruction methods.

Four reconstruction approaches with different representatives of multilayer sections are evaluated. The registration pipeline introduced in Section II-B is adopted. Without tissue flattening and SIP, the registration pipeline with the MIP of each section serves as the baseline method (MIP). After tissue flattening, the top and the bottom layers are used as the representatives for registration in the second version (Surface). As the motivation of the proposed SIP, BRS [25] is evaluated by selecting the best representatives from flattened multilayer sections (BRS [25]). At last, the fourth version includes both tissue flattening and SIP. The propagated top

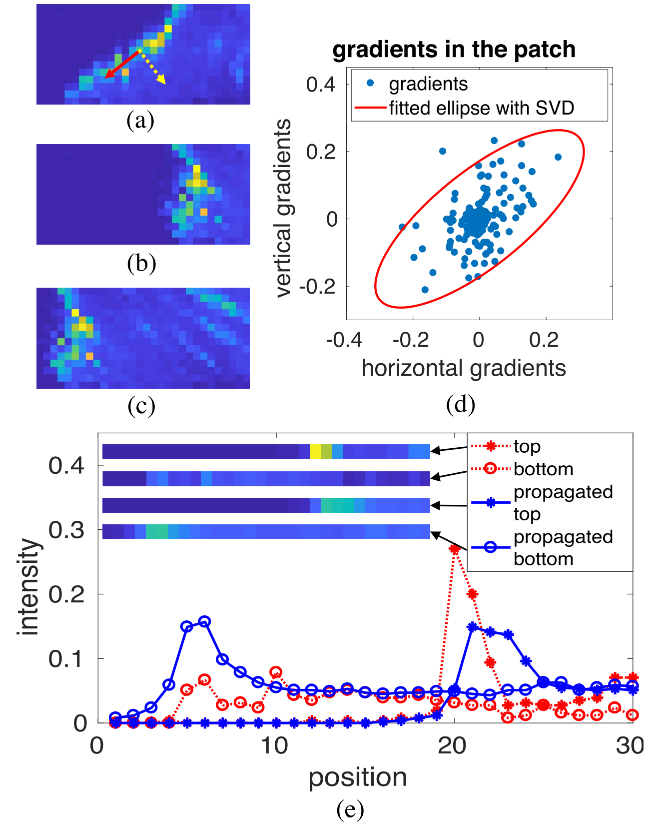

Fig. 5. An illustration of the structure-based intensity propagation on the 2D case. (a) is a cross-section view of the raw data. The solid arrow indicates the structure direction, and the dashed arrow corresponds to the normal direction. (b) and (c) are the stacks after transforming each lines to the surface positions, equivalent to I^{top} and I^{bottom} in Alg. 1. (d) plots the gradients in (a) and illustrates the SVD operation. The propagated surface lines reflect the positions of boundaries more accurately.

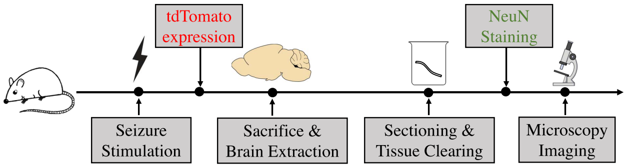

Fig. 6. Data collection procedure. The red fluorescent markers are expressed during seizure spread while the mice are alive. After sacrificing animals, immunofluorescence staining for NeuN is performed.

and bottom surfaces are used for registration in the fourth version (SIP). The patch size, N, in Alg. 1 is set as 51 for all the experiments. The raw data is acquired with the resolution of $2.77 \times 2.77 \times 10\ \mu m^3$, and is scaled to $10 \times 10 \times 10\ \mu m^3$ with cubic interpolation [42] before reconstruction.

A. Data Acquisition

In these experiments, a total of 367 sections from 20 TRAP mice [44] are collected according to the institutional animal care and use committee (IACUC) approved protocol. The data collection procedure is illustrated in Fig. 6. The geometric distortions mainly occur at the brain sectioning and tissue clearing steps. The vibratome used for tissue sectioning is the Leica vibratome VT1200, and the vertical deflection of the VT1200 is less than 1 μm [45]. When slicing tissues with the thickness of 200 μm, the vertical deflection is less than 1%. After brain sectioning, lipids are extracted from the tissue to increase the depth of light penetration by tissue clearing [34]. During tissue clearing, slices are incubated in 1% acrylamide, 0.25% VA044 solution with nitrogen under vacuum for 20 minutes, and then transferred to incubator with 37°C. This procedure builds the hydrogel-matrix needed for further clearing step. Slices are then cleared by incubation in 8% SDS buffer at 37°C. The cleared tissue is placed in refractive index matching solution (RIMS) for imaging. Two channels of fluorescent signal are collected. The red fluorescent protein, tdTomato, is expressed in the mouse brain during seizure spreading. After brain sectioning and clearing, tissues are stained for neuronal marker NeuN (green). Images are obtained using a Zeiss 780 confocal microscope with C-Apochromat objective under 10X magnification. Excitations for the green and the near-red are provided by Argon 488 and DPSS 561 laser lines, and the emission windows are 500-562 nm for the green and 571-624 nm for the near-red. All images are acquired with an optical section separation (z-interval) of 10 μm. Fig. 7 shows one section sample. Since the tdTomato channel has higher signal intensity and contrast, the following reconstructions are based on the information from the tdTomato channel.

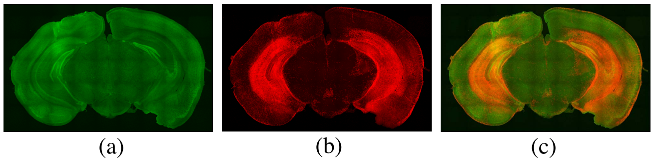
(a) (b) (c)

Fig. 7. (a) NeuN. (b) tdTomato. (c) Aligned two channels. All three images, (a), (b) and (c), are sections on the coronal plane.

B. Evaluation Criteria

Evaluating the quality of reconstructed brains is challenging because the lack of ground truth [9], [25], [27]. Visual inspection, manually selected landmarks, and structure smoothness are three commonly used evaluation approaches. Visual inspection of 3D volumes requires extensive human intervention [9], [24]. Similarly, evaluation with manually selected landmarks is not scalable [28]. The third evaluation metric based on the structure smoothness can be further classified into texture-based [46]–[48] and feature-based [26], [49], [50]. Texture-based metrics are not suitable for reconstruction evaluation with multilayer sections. The quality of reconstructed brains with multilayer sections is reflected at the interfaces between two physical sections, while texture-based metrics equally weight patches and tend to be influenced by the false texture at section joints. Since our work aims at registering multilayer sections to each other, the edge-based tensor voting evaluation [51] is most suitable to reflect the structure consistence among multilayer sections. In addition, this metric differs from the cost functions adopted by our registration methods, and thus is more objective.

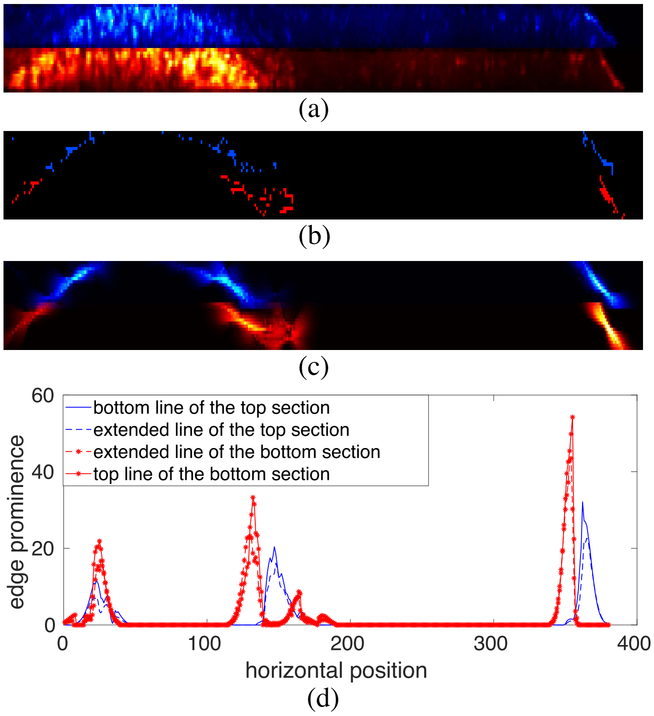

Fig. 8. (a) is a cross-section view of two aligned sections. (b) is the cross-section view of extracted edges. (c) is the edge prominence map voted by edge points in (b). The structures in the top section extend one layer downward, and the structures in the bottom section extend one layer upward. Therefore, the edge prominence in the top section and the bottom section has two layers overlapped in (c). (d) plots the edge prominence in overlapped layers in (c).

Fig. 8 illustrates the three steps of the evaluation scheme [49]: token extraction, tensor voting and correlation. Tokens are the points that lie on edges [49]. Edges are extracted on imaging planes, and Fig. 8(b) is the cross-section view of the 3D edge stack. In the second step of tensor voting, tokens communicate with each other and agree on a significant structure [49]. The output of token communication is referred as edge prominence as shown in Fig. 8(c). At last, the zero-normalized cross-correlation of the edge prominence at the overlapped regions is used as the structure consistence index for one cross-section view. Since the quality of the reconstructed brain is reflected by the cross-section views [18], [24], [26], the overall reconstruction quality is the average of the structure consistence indexes of all the cross-section views. Two key parameters for this evaluation metric are the tensor voting scale and the overlap range [49]. The larger the tensor voting scale, the blurrier the edge prominence map (Fig. 8(c)) will be. The tensor voting scale is set as 10, and the overlap range is set as 2 for the example in Fig. 8 and for all the following experiments.

C. Section-to-Section Alignment

In this experiment, all the sections are flipped according to the manually labeled ground truth before registration. The adjacent section pairs are aligned to each other with the four different representatives of the multilayer sections: MIP, Surface, BRS and SIP. The sections are classified by their imaging planes: horizontal plane and coronal plane. There are 134 pairs of adjacent sections in the group of horizontal plane, and 213 pairs in the group of coronal plane.

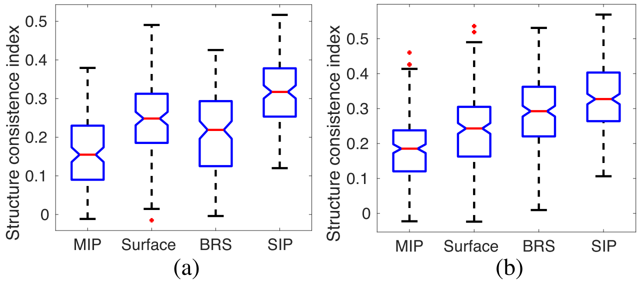

Fig. 9. Structure consistence index of registered section pairs. (a) Sections imaged on the horizontal plane. (b) Sections imaged on the coronal plane.

TABLE I

STRUCTURE CONSISTENCE INDEX OF SECTION-TO-SECTION ALIGNMENT

		MIP	Surface	BRS	SIP
Horizontal	Median	0.1536	0.2669	0.2167	**0.3172**
	Mean	0.1622	0.2681	0.2059	**0.3185**
Coronal	Median	0.1837	0.2562	0.2922	**0.3298**
	Mean	0.1829	0.2482	0.2870	**0.3355**

TABLE II

INCORRECT FLIP DETECTION NUMBER

		MIP	Surface	BRS	SIP
Horizontal (134)	Falsely flipped	2	26	2	**1**
	Falsely unflipped	**1**	16	3	**1**
Coronal (213)	Falsely flipped	8	42	4	**2**
	Falsely unflipped	7	25	7	**2**

Fig. 9 shows the quality of registered section pairs, and Table I summarizes the quantitative results. Single factor ANOVA is conducted to compare the performance of the four different multilayer representatives. The mean structure consistence indexes of these four methods are significantly different with $p < 10^{-36}$ for horizontal sections, and $p < 10^{-46}$ for coronal sections. Since sections are flipped according to the ground truth, this experiment mainly compares the accuracy of structure position reflected by different representatives. Maximum intensity projection of a multilayer section blends structures from different layers, and thus provides the lowest structure consistence index. After tissue flattening, structures in surface layers often show minor offsets compared with the structural trend exhibited by intra-section regions. Propagated surfaces correct such structure offsets in the surface layers and achieve the best alignment result. One interesting result is that the performances of Surface and BRS [25] are different on coronal and horizontal sections. This is because surface layers reflect the shape changing better than selected middle layers, and the shape growing trend is more significant among horizontal sections. However, the drawback of Surface is that the signal intensity and contrast are weak. The following auto-flip experiment demonstrates how this drawback affects the reconstruction.

Fig. 10 shows one example to illustrate how the proposed tissue flattening and SIP improve the performance of adjacent section alignment. Registered with MIP, two sections in

TABLE III
STRUCTURE CONSISTENCE INDEX OF WHOLE BRAIN RECONSTRUCTION

# Brain	Quality with flip groundtruth				Quality with auto-flip				# incorrect flip with auto-flip			
	MIP	Surface	BRS	SIP	MIP	Surface	BRS	SIP	MIP	Surface	BRS	SIP
1	0.2660	0.3184	0.2678	**0.4464**	0.2746	0.2820	0.2560	**0.4419**	2	12	6	**1**
2	0.2246	0.2922	0.2608	**0.3325**	0.2246	0.2760	0.2113	**0.3325**	**0**	9	13	**0**
3	0.1663	0.3145	0.2650	**0.3760**	0.1888	0.2574	0.2401	**0.3760**	9	10	10	**0**
4	0.2199	0.2308	0.2185	**0.3042**	0.2199	0.2213	0.1796	**0.3042**	**0**	4	12	**0**
5	0.1449	0.2419	0.1648	**0.2762**	0.1422	0.2250	0.2009	**0.2762**	4	6	7	**0**
6	0.2265	0.3064	0.2892	**0.3426**	0.2179	**0.3291**	0.2752	0.3064	18	**4**	10	16
7	0.2458	0.2812	0.2841	**0.3374**	0.1941	0.2675	0.2641	**0.3374**	18	10	5	**0**
8	0.1968	0.2468	0.2617	**0.2798**	0.1696	0.2262	0.2467	**0.2798**	10	11	6	**0**
9	0.2053	0.2729	0.2262	**0.2935**	0.1748	0.2596	0.1749	**0.2935**	13	8	7	**0**
10	0.3016	0.3016	0.3667	**0.4215**	0.2348	0.2763	0.3478	**0.4215**	5	12	9	**0**
11	0.3991	0.3723	0.4079	**0.5240**	0.3991	0.3419	0.4079	**0.5240**	**0**	2	**0**	**0**
12	0.2647	0.3250	0.3441	**0.3996**	0.2952	0.3179	0.3426	**0.3996**	25	9	1	**0**
13	0.1953	0.2413	**0.3312**	0.2746	0.1762	0.2678	0.3073	**0.3097**	19	**9**	15	10
14	0.2257	0.2775	0.3371	**0.3636**	0.1987	0.2762	0.3043	**0.3636**	20	11	21	**0**
15	0.2021	0.3236	0.3215	**0.3668**	0.2049	0.3332	0.3322	**0.3571**	18	10	9	**3**
16	0.3000	0.2607	0.2480	**0.3406**	0.3124	0.2979	0.2619	**0.3406**	2	8	5	**0**
17	0.2841	0.2770	0.3031	**0.3205**	0.2841	0.2538	0.2720	**0.3205**	**0**	13	21	**0**
18	0.1868	0.3177	0.3367	**0.3564**	0.1690	0.3321	0.3022	**0.3520**	12	11	18	**3**
19	0.2341	0.3130	0.3410	**0.3541**	0.2510	0.2750	0.3098	**0.3541**	21	12	12	**0**
20	0.2291	0.2262	**0.3207**	0.2640	0.2298	0.2409	**0.2649**	0.2640	19	6	12	**0**
mean	0.2359	0.2871	0.2948	**0.3487**	0.2281	0.2779	0.2751	**0.3477**	10.75	8.85	9.95	**1.65**

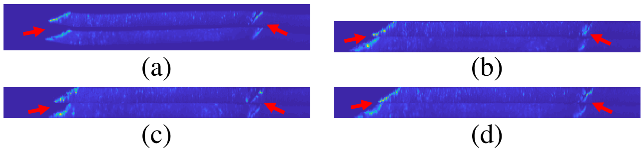
(a) (b) (c) (d)

Fig. 10. Examples of section-to-section registration with four different representatives. (a) MIP. (b) Surface. (c) BRS [25]. (d) Proposed SIP.

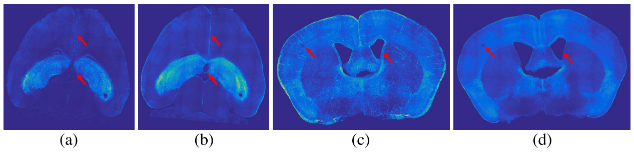
(a) (b) (c) (d)

Fig. 11. The surface layer after tissue flattening in (a) shows less signal intensity and structure contrast compared with the propagated surface in (b). Compared with the maximum intensity projection in (c), the propagated surface in (d) removes the structures that only stay in certain layers and preserves the major structures. (a) and (b) are sections on the horizontal plane. (c) and (d) are sections on the coronal plane.

Fig. 10(a) pose a noticeable offset. Minor offsets still exist in the aligned sections with surface layers, but is corrected by the structure-based intensity propagation. The best reference layers selected by BRS [25] are the 10th and the 8th layers for the first and the second multilayer sections, and therefore the registration does not capture the growing trend.

D. Flip Detection

Although experimenters carefully track and label orientations of sections, inconsistencies can happen during large data collection, especially when tissue clearing is involved. Among the 367 raw sections in our experiment, 169 sections (46%) are flipped according to the ground truth. Incorrectly flipped sections are a major source of artifacts in brain reconstruction, especially for whole brain reconstruction with a series of sections: one incorrectly flipped section may influence flip decisions of all the following sections.

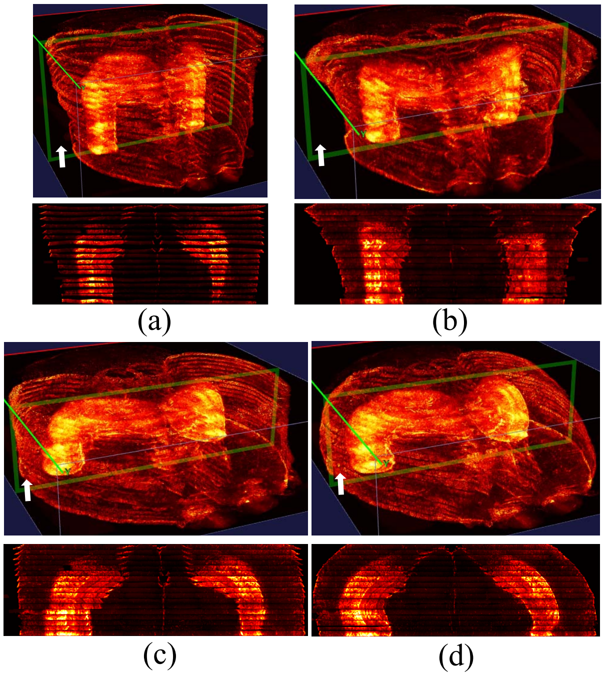
(a) (b) (c) (d)

Fig. 12. Reconstructed Brain 1, sectioned on the horizontal plane. The arrows indicate the ventral-dorsal direction. The frames indicate the positions of the cross-section views. The cross-section views are on the coronal plane. (a) MIP: 0.2746. (b) Surface: 0.2820. (c) BRS: 0.2560. (d) SIP: 0.4419.

In this part, automatic flip detections with different representatives of multilayer sections are compared. Adjacent sections are registered, but only the first section is flipped according to the ground truth. The flip status of the second section is automatically decided according to affine registration results.

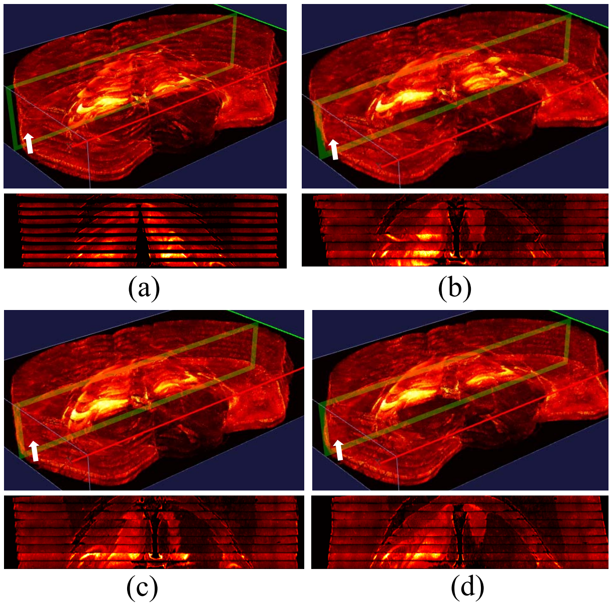

Fig. 13. Reconstructed Brain 11, sectioned on the coronal plane. The arrows indicate the posterior-anterior direction. The frames indicate the positions of the cross-section views. The cross-section views are on the horizontal plane. (a) MIP: 0.3991. (b) Surface: 0.3419. (c) BRS: 0.4079. (d) SIP: 0.5240.

In this experiment, flip detection is evaluated for each section pair, and one incorrect flip decision does not influence the following flip decisions. Table II reports the flip detection results of the four versions in terms of Type I error (falsely flipped sections) and Type II error (falsely unflipped sections). Flip detection based on the propagated surfaces achieves highest accuracy. An interesting phenomenon is that Surface achieves much worse flip detection accuracy than others. This is because although surface layers reflect the shape changing more accurately, they do not preserve the intensity information well. For flip detection, the asymmetric intensity information is crucial.

Fig. 11 shows different multilayer section representatives for flip detection. Compared with the propagated surface in Fig. 11(b), the surface layer in Fig. 11(a) lessens structure contrast. On the contrary, the maximum intensity projection in Fig. 11(c) contains many structures that could mislead flip detection, such as the neurons. Only propagated surface layers preserve the consistent information among sections that is helpful to flip detection, and also get rid of the distracting information that only shows in certain layers.

E. Whole Brain Reconstruction

In this part, 20 mouse brains are reconstructed with and without the ground truth of flip status. Table III summarizes the reconstruction quality by different approaches. The same structure consistence index introduced in Section IV-B is adopted to measure the whole brain reconstruction quality. As stated before, for the whole brain reconstruction, one wrong flip can influence the following flips. Therefore, a wrong flip at the beginning tends to cause more incorrect flip detections in the following sections, such as the sixth brain reconstructed with the propagated surface. Single factor ANOVA confirms that the difference between the four reconstruction approaches is significant with $p < 10^{-7}$ for the 20 brains. Fig. 12 and Fig. 13 show two examples of the reconstructed brains with automatic flip detection. Brain reconstruction with propagated surfaces improves the reconstruction quality in two aspects: more natural outer contour shape from the 3D overview and more consistent structure changing from the cross-section views.

V. CONCLUSION

In this paper, two structure correction methods are proposed for brain reconstruction with multilayer tissue sections: tissue flattening and structure-based intensity propagation. Tissue flattening projects the warped multilayer sections onto the bottom surfaces. Structure-based intensity propagation extends the intensity information within 3D section to surface layers. After tissue flattening and structure-based intensity propagation, the propagated surfaces serve as robust representatives of multilayer tissue sections, and facilitate the following registration and flip detection. The proposed methods can be incorporated into existing registration-based reconstruction frameworks as a preprocessing step. Experiments on 367 brain sections from 20 mouse brains verify the effectiveness of the proposed methods. Section-to-section experiments evaluate the performance improvement on registration and flip detection by the proposed methods. The whole brain reconstruction is evaluated in the last experiment. Because the propagated surfaces accurately reflect the structural trends and preserve the intensity distribution in multilayer sections, 3D volume reconstruction of other tissues imaged with confocal microscopy also would likely benefit from the proposed structure correction methods.

In the future, we will keep working on 3D brain reconstruction in two directions. First, multi-scale information can be incorporated to improve the speed and robustness of the current methods. Second, anatomical structures can be labeled by atlas-matching.

REFERENCES

[1] S. W. Paddock ed and K. W. Eliceiri, "Laser scanning confocal microscopy: History, applications, and related optical sectioning techniques," in *Confocal Microscopy*. vol. 1075. New York, NY, USA: Humana Press, 2014, pp. 9–47.

[2] N. Pritchard, K. Edwards, A. W. Russell, B. A. Perkins, R. A. Malik, and N. Efron, "Corneal confocal microscopy predicts 4-year incident peripheral neuropathy in type 1 diabetes," *Diabetes Care*, vol. 38, no. 4, pp. 671–675, 2015.

[3] J. Dauguet *et al.*, "Three-dimensional reconstruction of stained histological slices and 3D non-linear registration with *in-vivo* MRI for whole baboon brain," *J. Neurosci. Methods*, vol. 164, no. 1, pp. 191–204, 2007.

[4] T. Ju, "Building a 3D atlas of the mouse brain," Dept. Comput. Sci., Rice Univ., Houston, TX, USA, Tech. Rep. 1549, 2005.

[5] R. Tomer, L. Ye, B. Hsueh, and K. Deisseroth, "Advanced CLARITY for rapid and high-resolution imaging of intact tissues," *Nature Protocols*, vol. 9, no. 7, pp. 1682–1697, 2014.

[6] E. S. Lein *et al.*, "Genome-wide atlas of gene expression in the adult mouse brain," *Nature*, vol. 445, no. 7124, pp. 168–176, 2007.

[7] S. W. Oh *et al.*, "A mesoscale connectome of the mouse brain," *Nature*, vol. 508, no. 7495, pp. 207–214, 2014.

[8] M. J. Hawrylycz *et al.*, "An anatomically comprehensive atlas of the adult human brain transcriptome," *Nature*, vol. 489, no. 7416, pp. 391–399, 2012.

[9] M. L. Berlanga *et al.*, "Three-dimensional reconstruction of serial mouse brain sections: Solution for flattening high-resolution large-scale mosaics," *Frontiers Neuroanatomy*, vol. 5, no. 17, pp. 1–8, Mar. 2011.

[10] T. Rohlfing, R. Brandt, R. Menzel, and C. R. Maurer, Jr., “Evaluation of atlas selection strategies for atlas-based image segmentation with application to confocal microscopy images of bee brains,” *NeuroImage*, vol. 21, no. 4, pp. 1428–1442, Apr. 2004.

[11] T. R. Brazelton, F. M. V. Rossi, G. I. Keshet, H. M. Blau, “From marrow to brain: Expression of neuronal phenotypes in adult mice,” *Science*, vol. 290, no. 5497, pp. 1775–1779, 2000.

[12] M. N. Economo *et al.*, “A platform for brain-wide imaging and reconstruction of individual neurons,” *Elife*, vol. 5, p. 10566, Jan. 2016.

[13] J. W. Bohland *et al.*, “A proposal for a coordinated effort for the determination of brainwide neuroanatomical connectivity in model organisms at a mesoscopic scale,” *PLoS Comput. Biol.*, vol. 5, no. 3, p. 1000334, pp. 1–9, 2009.

[14] W. M. Abdelmoula *et al.*, “Automatic registration of mass spectrometry imaging data sets to the allen brain atlas,” *Anal. Chem.*, vol. 86, no. 8, pp. 3947–3954, 2014.

[15] A. Osokin, D. Vetrov, and D. Kropotov, “3-D mouse brain model reconstruction from a sequence of 2-D slices in application to Allen brain atlas,” in *Proc. Int. Meeting Comput. Intell. Methods Bioinf. Biostatistics*. Berlin, Germany: Springer, 2009, pp. 291–303.

[16] P. R. Hof, *Comparative Cytoarchitectonic Atlas of the C57BL/6 and 129/SV Mouse Brains*. Amsterdam, The Netherlands: Elsevier, 2000.

[17] G. Paxinos and K. B. J. Franklin, *The Mouse Brain in Stereotaxic Coordinates: Compact*, 2nd ed. Houston, TX, USA: Gulf Professional Publishing, 2004.

[18] S. Ourselin, A. Roche, G. Subsol, X. Pennec, and N. Ayache, “Reconstructing a 3D structure from serial histological sections,” *Image Vis. Comput.*, vol. 19, nos. 1–2, pp. 25–31, 2001.

[19] N. Renier *et al.*, “iDISCO: A simple, rapid method to immunolabel large tissue samples for volume imaging, ” *Cell*, vol. 159, no. 4, pp. 896–910, 2014.

[20] D. GoodSmith *et al.*, “Spatial representations of granule cells and mossy cells of the dentate gyrus,” *Neuron*, vol. 93, no. 3, pp. 677–690, 2017.

[21] J. P. Neunuebel and J. J. Knierim, “CA3 retrieves coherent representations from degraded input: Direct evidence for CA3 pattern completion and dentate gyrus pattern separation,” *Neuron*, vol. 81, no. 2, pp. 416–427, Jan. 2014.

[22] E. T. Rolls, “The mechanisms for pattern completion and pattern separation in the hippocampus,” *Frontiers Syst. Neurosci.*, vol. 7, no. 74, pp. 1–21, Oct. 2013.

[23] M. Stille, E. J. Smith, W. R. Crum, and M. Modo, “3D reconstruction of 2D fluorescence histology images and registration with *in vivo* MR images: Application in a rodent stroke model,” *J. Neurosci. Methods*, vol. 219, no. 1, pp. 27–40, 2013.

[24] P. A. Yushkevich *et al.*, “3D mouse brain reconstruction from histology using a coarse-to-fine approach,” in *Proc. Int. Workshop Biomed. Image Registration*. Berlin, Germany: Springer, 2006, pp. 230–237.

[25] U. Bagci and L. Bai, “Automatic best reference slice selection for smooth volume reconstruction of a mouse brain from histological images,” *IEEE Trans. Med. Imag.*, vol. 29, no. 9, pp. 1688–1696, Sep. 2010.

[26] T. Ju *et al.*, “3D volume reconstruction of a mouse brain from histological sections using warp filtering,” *J. Neurosci. Methods*, vol. 1, no. 156, pp. 84–100, Feb. 2006.

[27] A. Cifor, L. Bai, and A. Pitiot, “Smoothness-guided 3-D reconstruction of 2-D histological images,” *NeuroImage*, vol. 56, no. 1, pp. 197–211, 2011.

[28] M. Čapek, P. Bruža, J. Janácek, P. Karen, L. Kubínová, and R. Vagnerová, “Volume reconstruction of large tissue specimens from serial physical sections using confocal microscopy and correction of cutting deformations by elastic registration,” *Microscopy Res. Techn.*, vol. 72, no. 2, pp. 110–119, 2009.

[29] P. Karen, M. Jirkovská, Z. Tomori, E. Demjénová, J. Janácek, and L. Kubínová, “Three-dimensional computer reconstruction of large tissue volumes based on composing series of high-resolution confocal images by GlueMRC and LinkMRC software,” *Microscopy Res. Techn.*, vol. 65, no. 5, pp. 415–422, 2003.

[30] S. Ghosh *et al.*, “Sensory maps in the olfactory cortex defined by long-range viral tracing of single neurons,” *Nature*, vol. 472, no. 7342, pp. 217–222, 2011.

[31] K. J. Hayworth *et al.*, “Ultrastructurally smooth thick partitioning and volume stitching for large-scale connectomics,” *Nature Methods*, vol. 12, no. 4, pp. 319–322, 2015.

[32] H. Liang, N. Dabrowska, J. Kapur, and D. S. Weller, “Whole brain reconstruction from multilayered sections of a mouse model of status epilepticus,” in *Proc. IEEE Asilomar Conf. Signals, Syst., Comput.*, Oct./Nov. 2017, pp. 1260–1263.

[33] C. Kenwright, É. Bardinet, S. A. Hojjat, G. Malandain, N. Ayache, and A. C. F. Colchester, “2-D to 3-D refinement of post mortem optical and MRI Co-registration,” in *Proc. MICCAI*, 2003, pp. 935–944.

[34] B. Yang *et al.*, “Single-cell phenotyping within transparent intact tissue through whole-body clearing,” *Cell*, vol. 158, no. 4, pp. 945–958, 2014.

[35] Y. I. Douglas, S. Richardson, C. Dulac, and J. Bergan, “Optimized protocol for imaging cleared neural tissues using light microscopy,” in *Synapse Development*. New York, NY, USA: Humana Press, 2017, pp. 137–153.

[36] M. R. Cronan, *et al.*, “CLARITY and PACT-based imaging of adult zebrafish and mouse for whole-animal analysis of infections,” *Disease Models Mech.*, vol. 8, no. 12, pp. 1643–1650, 2015.

[37] D. S. Richardson and J. W. Lichtman, “Clarifying tissue clearing,” *Cell*, vol. 162, no. 2, pp. 246–257, 2015.

[38] S. Ohno *et al.*, “A morphological analysis of thalamocortical axon fibers of rat posterior thalamic nuclei: A single neuron tracing study with viral vectors,” *Cerebral Cortex*, vol. 22, no. 12, pp. 2840–2857, 2011.

[39] A. Roche, G. Malandain, X. Pennec, and N. Ayache, “The correlation ratio as a new similarity measure for multimodal image registration,” in *Proc. MICCAI*, 1998, pp. 1115–1124.

[40] F. Maes, A. Collignon, D. Vandermeulen, G. Marchal, and P. Suetens, “Multimodality image registration by maximization of mutual information,” *IEEE Trans. Med. Imag.*, vol. 16, no. 2, pp. 187–198, Apr. 1997.

[41] A. Myronenko and X. Song, “Intensity-based image registration by minimizing residual complexity,” *IEEE Trans. Med. Imag.*, vol. 29, no. 11, pp. 1882–1891, Nov. 2010.

[42] R. G. Keys, “Cubic convolution interpolation for digital image processing,” *IEEE Trans. Acoust., Speech, Signal Process.*, vol. ASSP-29, no. 6, pp. 1153–1160, Dec. 1981.

[43] A. F. Frangi, W. J. Niessen, K. L. Vincken, and M. A. Viergever, “Multiscale vessel enhancement filtering,” in *Medical Image Computing and Computer-Assisted Intervention—MICCAI*. Berlin, Germany: Springer, 1998, pp. 130–137.

[44] C. J. Guenthner, K. Miyamichi, H. H. Yang, H. C. Heller, and L. Luo, “Permanent genetic access to transiently active neurons via trap: Targeted recombination in active populations,” *Neuron*, vol. 78, no. 5, pp. 773–784, 2013.

[45] D. M. Mathis, J. L. Furman, and C. M. Norris, “Preparation of acute hippocampal slices from rats and transgenic mice for the study of synaptic alterations during aging and amyloid pathology,” *J. Visualized Exp.*, no. 49, p. e2330, 2011.

[46] M. Capek, J. Janacek, and L. Kubinova, “Methods for compensation of the light attenuation with depth of images captured by a confocal microscope,” *Microscopy Res. Techn.*, vol. 69, no. 8, pp. 624–635, 2006.

[47] G. N. Laszlo and J. Udupa, “On standardizing the mr image intensity scale,” *Magn. Reson. Med.*, vol. 42, no. 6, pp. 1072–1081, 1999.

[48] A. Madabhushi and J. K. Udupa, “New methods of MR image intensity standardization via generalized scale,” *Med. Phys.*, vol. 33, no. 9, pp. 3426–3434, 2006.

[49] M. Yigitsoy and N. Navab, “Structure propagation for image registration,” *IEEE Trans. Med. Imag.*, vol. 32, no. 9, pp. 1657–1670, Sep. 2013.

[50] E. Guest and R. Baldock, “Automatic reconstruction of serialsections using the finite element method,” *Bioimaging*, vol. 3, no. 4, pp. 154–167, 1995.

[51] G. Medioni, C.-K. Tang, and M.-S. Lee, “Tensor voting: Theory and applications,” in *Proc. Reconnaissance Formes Intell. Artificielle*, 2000, pp. 1–10.